Efficient quantum state tomography with Chebyshev polynomials

Hao Su
State Key Laboratory for Turbulence and Complex Systems, School of Mechanics and Engineering Science, Peking University, Beijing 100871, China

Shiying Xiong*
Department of Engineering Mechanics, School of Aeronautics and Astronautics, Zhejiang University, Hangzhou 310027, China

Yue Yang†
State Key Laboratory for Turbulence and Complex Systems, School of Mechanics and Engineering Science, Peking University, Beijing 100871, China
and HEDPS-CAPT, Peking University, Beijing 100871, China

(Received 2 September 2025; accepted 13 March 2026; published 27 April 2026)

Quantum computing shows promise for addressing computationally intensive problems, but is constrained by the exponential resource requirements of general quantum state tomography (QST), which fully characterizes quantum states through parameter estimation. We introduce the QST with Chebyshev polynomials, an approximate tomography method for pure quantum states encoding complex-valued functions. This method reformulates tomography as the estimation of Chebyshev expansion coefficients, expressed as the inner products between the target quantum state and Chebyshev basis functions, measured using the Hadamard test circuit. By treating the truncation order of the Chebyshev polynomials as a controllable parameter, the method provides a practical balance between efficiency and accuracy. For quantum states' encoding functions dominated by large-scale features, such as those representing fluid flow fields, appropriate truncation enables faithful reconstruction of the dominant components via quantum circuits with linear depth, while keeping both measurement repetitions and postprocessing independent of qubit count, in contrast to the exponential scaling of full measurement-based QST methods. Validation on analytic functions and numerically generated flow-field data demonstrates accurate reconstruction and effective extraction of large-scale features, indicating the method's suitability for systems governed by macroscopic dynamics.

DOI: 10.1103/9l5c-hvnt

I. INTRODUCTION

Quantum computing has drawn increasing attention in recent years owing to its capacity for exponential data storage and its potential to accelerate various algorithms [1–6]. For classical physical systems, quantum computing offers a pathway to enhance the numerical solution of models such as differential equations by mapping their discretized forms into quantum-linear algebraic problems, where quantum algorithms may provide advantages in high-dimensional scaling, sampling efficiency, and measurement strategies tailored to specific objectives. In particular, quantum computing for fluid dynamics (QCFD) is an emerging field that seeks to solve classical fluid mechanics problems using quantum approaches [7–10]. Despite the development of various frameworks and algorithms [11–25], few can be effectively implemented on current quantum devices, partly restrained by the quantum state tomography (QST) complexity.

A quantum state fully characterizes a system, with pure states described as vectors in Hilbert space and general states represented by density matrices that encode both pure and mixed states. Quantum measurements are intrinsically probabilistic, collapsing the state into an eigenstate of the measurement operator. QST reconstructs the full state by performing repeated measurements on an ensemble of identical states, which, together with Born's rule [1], allows the reconstruction of a density matrix consistent with the observed data. It is indispensable for verifying state preparation fidelity and characterizing algorithm outputs.

Despite its importance, QST faces major challenges in practical settings, where quantum algorithms often involve processing large datasets and require dense amplitude encoding across many qubits. In such cases, the number of parameters needed to describe the quantum state grows exponentially, resulting in significant computational overhead that can offset the expected advantages of quantum algorithms [26,27]. This scaling issue makes full state reconstruction computationally expensive and impractical for large systems, limiting the broader application of quantum algorithms in fields such as QCFD and simulations of other complex systems.

Multiple QST methods have been developed to address these challenges, including maximum-likelihood estimation [28,29], gradient-based optimization [30,31], machine learning approaches [32–34], linear regression estimations

*Contact author: shiying.xiong@zju.edu.cn
†Contact author: yyg@pku.edu.cn

[35–37], and other advanced schemes [38–40]. More efficient methods can be established if extra restrictions are imposed on the quantum states. Examples include compressed sensing [26,41] for low-rank density matrices and matrix product state (MPS) tomography [42,43] regarding low-dimensional productive density matrices, simplifying the reconstruction of entangled systems. Overall, these methods aim to find more concise expressions of certain quantum states to shrink down the parameter space, allowing for more efficient state reconstruction in specific contexts.

We present the QST with Chebyshev polynomials (QST-CP), a spectral approach that incorporates scale information through Chebyshev polynomial decomposition. Each Chebyshev basis function represents a scale-dependent mode and prioritizes large-scale structures over finer-scale details. Low-order modes capture the large-scale, energetically dominant features of the encoded function, while higher-order modes describe finer-scale variations. This hierarchical organization naturally supports effective truncation, as retaining only the most informative modes allows the essential physical content of the state to be preserved while mitigating the measurement overhead required for QST. A similar approach can also be found in quantum chemistry [44,45], where localized Lorentzian functions are utilized as a basis set to achieve efficient quantum encoding.

The QST-CP is applied to pure quantum states encoding continuous functions, commonly arising in solving differential equations [4,46,47], where solutions are encoded in the amplitudes of a quantum state. By expanding these functions in terms of Chebyshev polynomials, we map the target function into a subspace spanned by a truncated Chebyshev series. The expansion coefficients, defined as inner products between the target function and the basis polynomials, are then measured via quantum circuits, as illustrated in Fig. 1. Given the quantum state encoding the target function in Fig. 1(a) together with the Chebyshev polynomial expansions in Fig. 1(b), the quantum circuit shown in Fig. 1(c) is employed to measure the expansion coefficients, from which the quantum state is reconstructed, as shown in Fig. 1(d). QST-CP provides a balance between efficiency and accuracy by adjusting the truncation length of the polynomial series. Short truncations significantly improve QST efficiency and retain large-scale modes, while longer truncations capture finer details at the cost of increased measurement expense. Validations are performed by reconstructing analytic functions and complex flow fields, demonstrating the robustness and efficacy of QST-CP in quantum state reconstruction [48].

This paper is structured as follows. The theoretical framework of QST-CP is introduced in Sec. II, and the corresponding circuit implementation is described in Sec. III. Numerical demonstrations are presented in Sec. IV, and concluding remarks are given in Sec. V.

II. QST WITH CHEBYSHEV POLYNOMIALS

A. QST on subspace

For a system of n qubits, the underlying Hilbert space is $\mathcal{H} = (\mathbb{C}^2)^{\otimes n}$ with dimension 2^n, where $\mathbb{C}$ denotes the complex plane. Physically distinct pure states correspond to the complex projective space $\mathbb{CP}^{2^n-1}$, obtained by identifying normalized vectors in $\mathcal{H}$ that differ only by a global phase. A general quantum state is described by a density operator $\varrho \in \mathcal{B}(\mathcal{H})$, where $\mathcal{B}(\cdot)$ denotes the space of bounded linear operator. Density operator ϱ is a $2^n \times 2^n$ Hermitian, positive semidefinite operator with unit trace, and its set forms a convex subset of $\mathbb{R}^{(2^n)^2-1}$. Hence, an n-qubit state is characterized by $4^n - 1$ independent real parameters.

The QST aims to reconstruct ϱ by performing measurements in different bases and estimating the outcome probabilities from Born's rule. Since the number of free parameters grows exponentially with n, standard QST typically requires on the order of 4^n measurement settings, rendering it impractical for large systems.

In many applications the relevant quantum states are not arbitrary but encode structured data. Consider a continuous function $f(x_1, \ldots, x_d)$ discretized on a grid of size $2^{n_1} \times \cdots \times 2^{n_d}$ with coordinates $(x_{k_1}, \ldots, x_{k_d})$. Its quantum state can be expressed as

$$|\psi\rangle = \sum_{k_1=0}^{2^{n_1}-1} \cdots \sum_{k_d=0}^{2^{n_d}-1} f\big(x_{k_1}, \ldots, x_{k_d}\big)|k_1\rangle \otimes \cdots \otimes |k_d\rangle. \quad (1)$$

Such state representations naturally arise in quantum algorithms for solving differential equations [4,46,47] and in QCFD, where solutions are stored in state amplitudes and efficient readout is essential. Many physically relevant functions exhibit scale-dependent behavior, allowing for the reconstruction of only a subset of amplitudes instead of performing full tomography on all of them. For instance, turbulent velocity fields follow the Kolmogorov theory [49], where the energy spectrum decays with wavenumber and obeys a power-law distribution in the inertial range. In such cases large-scale components dominate the overall behavior.

In classical approximation theory, continuous functions are represented using orthogonal bases. By expanding f in terms of Chebyshev polynomials and restricting the state to the subspace spanned by a truncated set of basis functions, one can retain the dominant large-scale content with relatively few coefficients. Tomography then reduces to estimating these coefficients, and such parametrization substantially lowers the measurement overhead while preserving the essential physical features of the quantum state.

B. Chebyshev polynomials

Chebyshev polynomials are a family of orthogonal polynomials that play an important role in approximation theory. They are frequently employed to represent continuous functions, for example, in numerical methods for differential equations, where physical quantities such as pressure, velocity, or temperature fields can be expanded using orthogonal polynomial bases.

The Chebyshev polynomial of degree p is defined as $T_p(x) = \cos(p \arccos x)$ for $-1 \leqslant x \leqslant 1$, and it satisfies the recurrence relation [50]

$$T_{p+1}(x) = 2xT_p(x) - T_{p-1}(x), \quad p \geqslant 1, \quad (2)$$

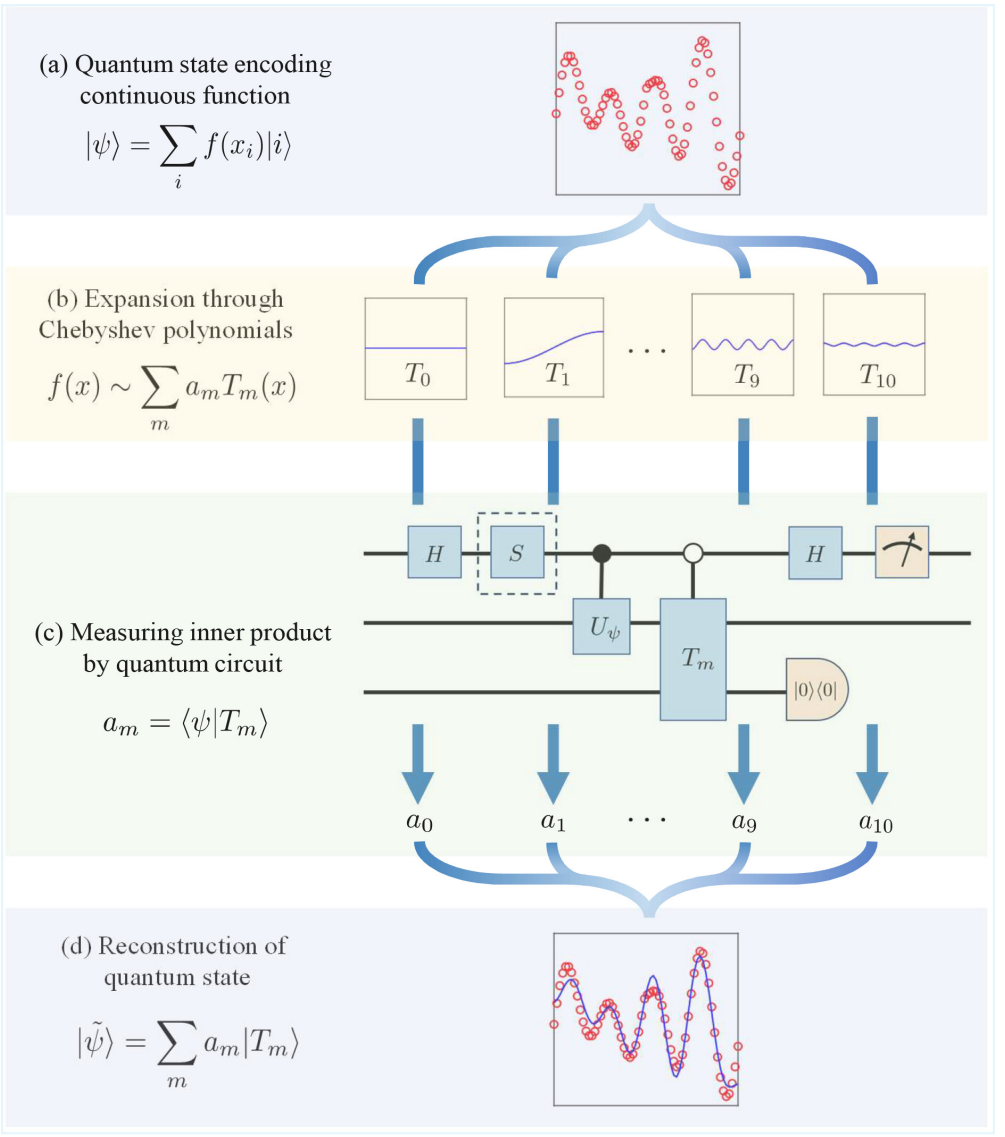

FIG. 1. Overview of QST-CP. (a) A pure quantum state encoding a continuous function $f(x)$. (b) Expansion of $f(x)$ using Chebyshev polynomials, truncated to approximate the original function. (c) Measurement of expansion coefficients as inner products between the target quantum state and Chebyshev basis functions via quantum circuits. (d) Reconstruction of the truncated series, enabling approximate tomography of the quantum state.

with initial conditions $T_0(x) = 1$ and $T_1(x) = x$. For example, $T_2(x) = 2x^2 - 1$, $T_3(x) = 4x^3 - 3x$, and $T_4(x) = 8x^4 - 8x^2 + 1$. The polynomial $T_p(x)$ has p distinct zeros in $[-1, 1]$, given by

$$X_{p,k} = \cos\frac{(2k+1)\pi}{2p}, \quad k = 0, \ldots, p-1, \tag{3}$$

which follow directly from the trigonometric definition. More generally, evaluating $T_p(x)$ at the zeros of $T_q(x)$ yields

$$T_p(X_{q,k}) = \cos\frac{(2k+1)p\pi}{2q}, \quad k = 0, \ldots, p-1. \tag{4}$$

Chebyshev polynomials satisfy a discrete orthogonality relation with respect to the set of zeros $\{X_{p,k}\}$ of T_p. Defining the discrete inner product as

$$\langle f, g\rangle_p \equiv \sum_{k=0}^{p-1} f(X_{p,k}) g(X_{p,k}),$$

the orthogonality relation reads

$$\langle T_s, T_t\rangle_p = \begin{cases} 0, & s \neq t, \\ p/2, & s = t \neq 0, \\ p, & s = t = 0, \end{cases} \tag{5}$$

for $0 \leqslant s, t \leqslant p$. Based on this, an orthonormal basis can be constructed as $\tilde{T}_{i,p}(x) \equiv T_i(x)/\sqrt{\langle T_i, T_i\rangle_p}$. Any function $f \in C([-1, 1])$, real- or complex-valued, can then be

approximated in terms of a truncated expansion

$$f(x) \sim f_P(x) = \sum_{s=0}^{P} a_s \tilde{T}_{s,p}(x), \quad a_s = \langle f, \tilde{T}_{s,p} \rangle_p,$$
$$0 \leqslant P \leqslant p-1. \tag{6}$$

The restriction $0 \leqslant P \leqslant p-1$ comes from the fact that f_{p-1} already accurately reproduces values on discrete points, as $f(X_{p,k}) = f_{p-1}(X_{p,k})$, and orthogonality relation fails for higher polynomial degrees. This expansion converges for piecewise continuous functions on $[-1, 1]$, and a classical error bound is available [51]: if $f^{(0)}, f^{(1)}, \ldots, f^{(r-1)}$ are absolutely continuous and $f^{(r)}$ has bounded variation V on $[-1, 1]$, then for $P > r$ the truncated series f_P satisfies $\max_{[-1,1]} |f(x) - f_P(x)| \leqslant 2V/[\pi r(P-r)^r]$. Hence the expansion achieves an algebraic convergence rate $O(P^{-r})$ for functions of sufficient smoothness, enabling approximate QST using truncated series.

As the Pth Chebyshev polynomial is defined by the cosine function and has P distinct zeros on the interval $[-1, 1]$, its corresponding length scale can be approximated as $2/P$. Therefore, for the truncated expansion $f_P(x)$ in Eq. (6), the finest length scale can be approximated as $2/P$.

The orthogonality extends naturally to multivariate functions through the tensor product basis $\tilde{T}_{s_1,p_1}(x_1) \cdots \tilde{T}_{s_d,p_d}(x_d)$. For $f(x_1, \ldots, x_d)$ on $[-1, 1]^d$, the expansion has the form

$$f(x_1, \ldots, x_d) \sim \sum_{s_1=0}^{P_1} \cdots \sum_{s_d=0}^{P_d} a_{s_1,\cdots,s_d} \tilde{T}_{s_1,p_1}(x_1) \cdots \tilde{T}_{s_d,p_d}(x_d),$$
$$0 \leqslant P_i \leqslant p_i - 1, \tag{7}$$

with expansion coefficients

$$a_{s_1,\cdots,s_d} = \left\langle f, \tilde{T}_{s_1,p_1} \cdots \tilde{T}_{s_d,p_d} \right\rangle_{p_1,\cdots,p_d}$$
$$\equiv \sum_{k_1=0}^{p_1-1} \cdots \sum_{k_d=0}^{p_d-1} f\left(X_{p_1,k_1}, \cdots, X_{p_d,k_d}\right) \tilde{T}_{s_1,p_1}\left(X_{p_1,k_1}\right)$$
$$\cdots \tilde{T}_{s_d,p_d}\left(X_{p_d,k_d}\right). \tag{8}$$

While exact function reconstruction requires the coefficients to match the number of grid points, smooth functions can be approximated using low-order terms that capture the large-scale behavior. The finest length scales for the dth direction can be similarly approximated as $2/P_d$. This mathematical structure motivates our quantum approach, where we efficiently extract expansion coefficients through quantum circuits to achieve approximate QST, thereby circumventing the traditional exponential costs.

III. IMPLEMENTATION OF QST-CP

A. QST-CP for single-variable functions

For single-variable functions, the quantum state in Eq. (1) simplifies to $|\psi\rangle = \sum_{k=0}^{2^n-1} f(x_k)|k\rangle$, where n is the number of qubits, k labels the computational basis states, and x_k denote uniformly spaced sampling points in $[-1, 1]$. To enable the Chebyshev expansion, we introduce a variable substitution $x_k \to X_{2^n,k}$, defining a new target function $F(X_{2^n,k}) = f(x_k)$. The quantum state then becomes $|\psi\rangle = \sum_{k=0}^{2^n-1} F(X_{2^n,k})|k\rangle$.

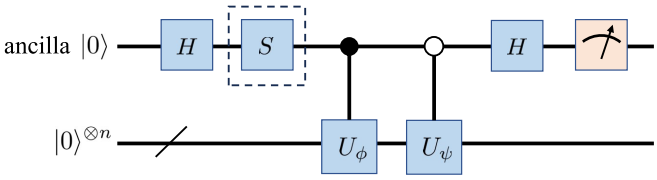

FIG. 2. Circuit for measuring inner product $\langle\phi|\psi\rangle$, where U_ϕ and U_ψ are the preparation circuits for $|\phi\rangle$ and $|\psi\rangle$. The measurement output switches between obtaining the real and imaginary parts of the inner product controlled by removal or inclusion of S gate enclosed by dashed line.

Note that if the original function $f(x)$ is defined on a region with length l_0, then the Pth degree truncation of the Chebyshev expansion will provide a length scale of l_0/P.

To measure $|\psi\rangle$, we introduce the normalized Chebyshev polynomials encoded by

$$|T_{s,n}\rangle = \sum_{k=0}^{2^n-1} \tilde{T}_{s,2^n}(X_{2^n,k})|k\rangle. \tag{9}$$

Thus the quantum state inner product equals the discrete polynomial inner product $\langle\cdot,\cdot\rangle_{2^n}$ with the following derivation:

$$\langle T_{s,n}|\psi\rangle = \sum_{k=0}^{2^n-1} \overline{\tilde{T}_{s,2^n}(X_{2^n,k})} F(X_{2^n,k}) = \sum_{k=0}^{2^n-1} \tilde{T}_{s,2^n}(X_{2^n,k}) F(X_{2^n,k})$$
$$= \langle F, \tilde{T}_{s,2^n} \rangle_{2^n},$$

where the second equality follows from the real-valued nature of $\tilde{T}_{s,2^n}(\cdot)$, allowing the expansion coefficients to be obtained directly via quantum state inner product measurements.

We employ the Hadamard test [1] presented in Fig. 2 to estimate this inner product. By removing or including the phase gate S in Fig. 2, the circuit is able to measure the real or imaginary part of the inner product, respectively. Given state preparation unitaries $|\phi\rangle = U_\phi|0\rangle$ and $|\psi\rangle = U_\psi|0\rangle$, we obtain $\text{Prob}(|0\rangle) = (1 + \text{Re}\langle\phi|\psi\rangle)/2$ without the S gate, and $\text{Prob}(|0\rangle) = (1 - \text{Im}\langle\phi|\psi\rangle)/2$ with the gate, where $\text{Prob}(|0\rangle)$ denotes the probability of obtaining output $|0\rangle$. This protocol separates estimations of both real and imaginary components of the inner product, extending QST-CP to general quantum states with complex amplitudes.

We prepare the state $|T_{s,n}\rangle$ using the Chebyshev polynomial values

$$T_s(X_{2^n,k}) = \cos\frac{(2k+1)s\pi}{2^{n+1}} \tag{10}$$

at the Chebyshev nodes $X_{2^n,k}$ via Eq. (4), where the normalization factor for $\tilde{T}_{s,2^n}$ is omitted here. The corresponding quantum circuit in Fig. 3 is inspired by the standard quantum Fourier transform circuit [1]. The controlled-gate segment generates the quantum state

$$|\psi\rangle = \frac{1}{2^{n/2}} \left(\sum_{k=0}^{2^n-1} e^{-ik\theta}|0\rangle \otimes |k\rangle + \sum_{k=0}^{2^n-1} e^{ik\theta}|1\rangle \otimes |k\rangle \right).$$

To convert the relative phase between the $|0\rangle$ and $|1\rangle$ components into a measurable amplitude difference in the computational register, subsequent application of the $P_{2\varphi}$ gate

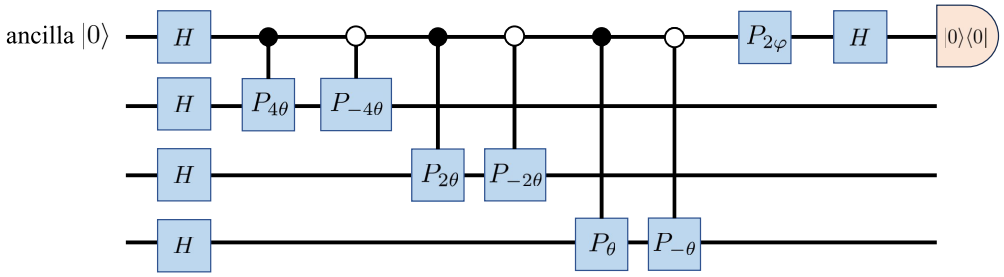

FIG. 3. Preparation circuit for $|T_{s,n}\rangle$ with $n = 3$, $\theta = s\pi/2^n$, and $\varphi = s\pi/2^{n+1}$. The $|0\rangle\langle 0|$ operation on the end of ancilla qubit refers to measuring the qubit so that the result is $|0\rangle$.

followed by a Hadamard gate to the ancilla qubit yields the state

$$\begin{aligned} HP_{2\varphi}|\psi\rangle &= \frac{1}{2^{n/2}} H\left(\sum_{k=0}^{2^n-1} e^{-ik\theta}|0\rangle\otimes|k\rangle + \sum_{k=0}^{2^n-1} e^{i(k\theta+2\varphi)}|1\rangle\otimes|k\rangle\right) \\ &= \frac{1}{2^{n/2}}\left(\sum_{k=0}^{2^n-1}\frac{1}{2}(e^{-ik\theta}+e^{i(k\theta+2\varphi)})|0\rangle\otimes|k\rangle + \sum_{k=0}^{2^n-1}\frac{1}{2}(e^{-ik\theta}-e^{i(k\theta+2\varphi)})|1\rangle\otimes|k\rangle\right) \\ &= \frac{1}{2^{n/2}}\left(e^{i\varphi}|0\rangle\otimes\sum_{k=0}^{2^n-1}\cos(k\theta+\varphi)|k\rangle + e^{i\varphi}|1\rangle\otimes\sum_{k=0}^{2^n-1}\sin(k\theta+\varphi)|k\rangle\right) \\ &= \frac{1}{2^{n/2}}\left(e^{i\varphi}|0\rangle\otimes\sum_{k=0}^{2^n-1}\cos\frac{(2k+1)s\pi}{2^{n+1}}|k\rangle + e^{i\varphi}|1\rangle\otimes\sum_{k=0}^{2^n-1}\sin\frac{(2k+1)s\pi}{2^{n+1}}|k\rangle\right), \end{aligned}$$

with substituting $\theta = s\pi/2^n$ and $\varphi = s\pi/2^{n+1}$. By selecting the $|0\rangle$ part of ancilla qubit, we reproduce the magnitude values specified in Eq. (10) up to an irrelevant global phase factor $e^{i\varphi}$.

The full circuit for the inner product measurement is presented in Fig. 4. We now analyze the possibility of operation $|0\rangle\langle 0|$ outputting $|0\rangle$, which is the success probability of state preparation. First, Eqs. (4) and (5) establish

$$\langle T_s, T_s\rangle_p = \sum_{k=0}^{p-1} T_s(X_{p,k})^2 = \sum_{k=0}^{p-1}\cos^2\frac{(2k+1)s\pi}{2p} = \frac{p}{2}.$$

Substituting $p = 2^n$ into this equation yields

$$\sum_{k=0}^{2^n-1}\cos^2\frac{(2k+1)s\pi}{2^{n+1}} = \sum_{k=0}^{2^n-1}\cos^2(k\theta+\varphi) = 2^{n-1}.$$

Then we have

$$\begin{aligned} \sum_{k=0}^{2^n-1}\sin^2(k\theta+\varphi) &= 2^n - \sum_{k=0}^{2^n-1}\cos^2(k\theta+\varphi) = 2^{n-1} \\ &= \sum_{k=0}^{2^n-1}\cos^2(k\theta+\varphi). \end{aligned}$$

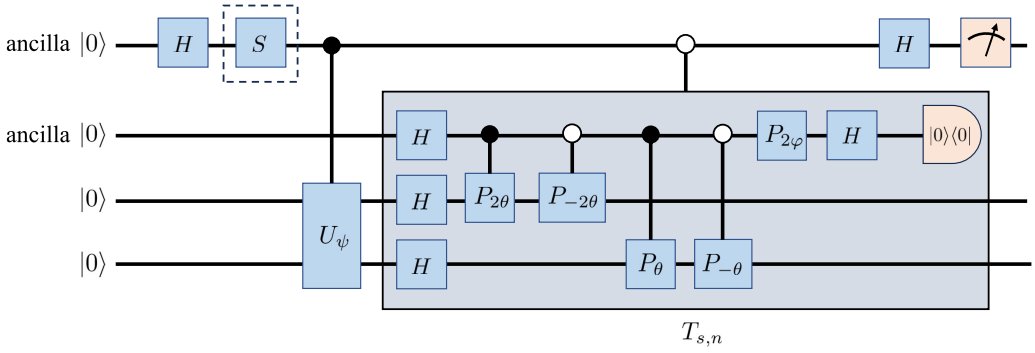

FIG. 4. The complete circuit for measuring the inner product $\langle T_{s,n}|\psi\rangle$, where we take $n = 2$; U_ψ is the preparation circuit for $|\psi\rangle$, and $T_{s,n}$ is the preparation circuit for the Chebyshev polynomial as shown in Fig. 3, with $\theta = s\pi/2^n$ and $\phi = s\pi/2^{n+1}$. The measurement output alternates between obtaining the real and imaginary parts of the inner product, controlled by the removal or inclusion of the S gate enclosed by the dashed lines.

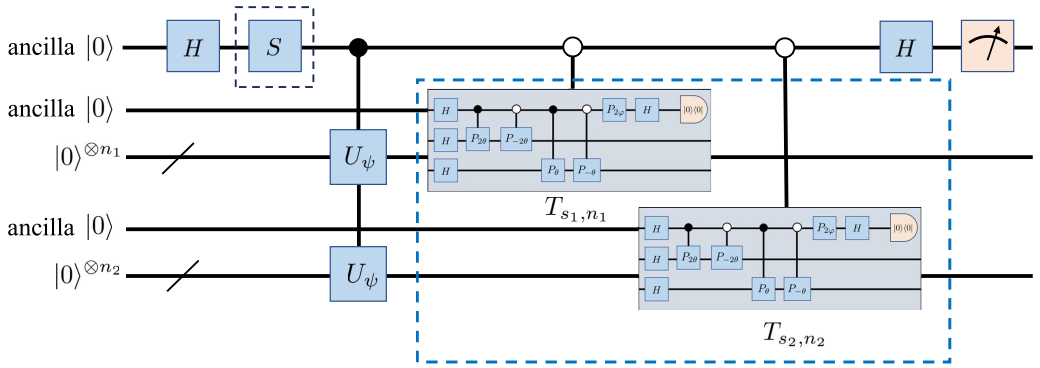

FIG. 5. Example of a circuit measuring the inner product between $|\psi\rangle$ and $|T_{s_1,n_1}\rangle \otimes |T_{s_2,n_2}\rangle$, where we take $n_1 = n_2 = 2$; U_ψ is the preparation circuit for $|\psi\rangle$, which is implemented on $|0\rangle^{\otimes n_1} \otimes |0\rangle^{\otimes n_2}$. The part enclosed by the dashed blue box is the preparation circuit of the multivariate polynomial basis $|T_{s_1,n_1}\rangle \otimes |T_{s_2,n_2}\rangle$, which consists of two parallel preparation circuits as shown in Fig. 3.

This implies that the ancilla qubit used to prepare $|T_{s,n}\rangle$ in Fig. 3 has an equal probability of collapsing to either $|0\rangle$ or $|1\rangle$. In the complete measurement circuit Fig. 4, the first ancilla qubit similarly exhibits equal probability of $|0\rangle$ and $|1\rangle$ after the initial Hadamard gate. Crucially, the $|T_{s,n}\rangle$ state preparation only occurs in the $|0\rangle$ branch. Consequently, the $|0\rangle\langle 0|$ measurement yields $|0\rangle$ with $\text{Prob}(|0\rangle) = 1-0.5\times 0.5 = 0.75$, i.e., the overall success probability for preparing $|T_{s,n}\rangle$ is 75%.

Theoretically, the inner product measurement can be extended up to the $(2^n - 1)$th-order polynomial, though this is computationally expensive and typically unnecessary in practice. To establish a stopping criterion for the measurement, we leverage the algebraic identity $\sum_{s=0}^{2^n-1} |a_s|^2 = \sum_{k=0}^{2^n-1} |f(x_k)|^2 = 1$, where the first equality mirrors Parseval's theorem, and the second follows from the quantum state normalization condition. We then define the partial sum

$$A_m \equiv \sum_{s=0}^{m} |a_s|^2 \leqslant 1 \tag{11}$$

to quantify the fraction of the original function's information captured by the Chebyshev expansion up to order m. By choosing a threshold value $A_c \in (0, 1)$, we stop the measurement procedure once $A_m \geqslant A_c$. This provides a simple and efficient stopping criterion, balancing efficiency and accuracy. Note that for a function encoded by n qubits, the highest polynomial order is $2^n - 1$, which corresponds to a lower bound of $2/(2^n - 1)$ on the characteristic length scale. The length scale of any truncated function cannot surpass this limit.

B. QST-CP for multivariable functions

For the multivariate case, we recall that $\{\tilde{T}_{s_1,p_1}(x_1)\ldots \tilde{T}_{s_d,p_d}(x_d)\}$ forms an orthonormal system. The corresponding quantum state admits the decomposition

$$\begin{aligned}\left|T_{s_1,\ldots,s_n,n_1,\ldots,n_d}\right\rangle = &\sum_{k_1=0}^{2^{n_1}-1} \cdots \sum_{k_d=0}^{2^{n_d}-1} \tilde{T}_{s_1,2^{n_1}}\left(X_{2^{n_1},k_1}\right) \\ &\cdots \tilde{T}_{s_d,2^{n_d}}\left(X_{2^{n_d},k_d}\right)|k_1\rangle \otimes \cdots \otimes |k_d\rangle \\ = &\left|T_{s_1,n_1}\right\rangle \otimes \cdots \otimes \left|T_{s_d,n_d}\right\rangle. \end{aligned} \tag{12}$$

This factorization infers that a multivariate Chebyshev polynomial can be prepared through parallel composition of single-variable circuits, as illustrated in Fig. 5.

The partial sum in Eq. (11) can be generalized to multivariate cases as

$$A_m \equiv \sum_{0\leqslant s_1+\cdots+s_d\leqslant m} \left|a_{s_1,\ldots,s_d}\right|^2, \tag{13}$$

where the summation runs over multiindices $(s_1, \ldots, s_n)$ with total degree not surpassing m. This yields a stopping criterion for multivariate measurements, where given a threshold $A_c \in (0, 1)$, we measure all inner products corresponding to mth-order polynomials and stop upon $A_m \geqslant A_c$. In other words, m required is related to the stopping criterion by

$$m = \arg\max_p \left(\sum_{s=0}^{p} |a_s|^2 \leqslant A_c\right) + 1. \tag{14}$$

C. Complexity analysis

We present a complexity analysis of QST-CP for measuring d-variable functions encoded using n qubits. The preparation circuit of $|T_{s,n}\rangle$ in Fig. 3 has a depth of $O(n)$, which is efficient. The introduction of control qubits to the preparation circuit U_ψ and $T_{s,n}$ in Fig. 4 adds extra circuit depth, with the amount of increase depending on the specific form of the preparation circuit for target state. Deep original circuits tend to introduce deep overhead and affect actual implementation. This can be alleviated by finding equivalent and shallower preparation circuits and searching for alternative inner product measurement methods.

The measurement repetition count mainly depends on the Chebyshev expansion order. For an mth-order expansion, the required number of Chebyshev bases scales as $O(m^d/d!)$. Furthermore, each basis preparation requires d extra measurements, each succeeding with probability 3/4. Thus, each basis demands $O[(4/3)^d/\varepsilon]$ measurement repetitions, and the total measurement count scales as $O[(4m/3)^d/(\varepsilon d!)]$, where ε denotes the error tolerance of the expansion coefficients, relative to their theoretical values. The polynomial degree m is related to the stopping criterion A_c by Eq. (14). The postprocessing only involves summing all employed Chebyshev bases with

TABLE I. The circuit depth, number of measuring repetitions, and postprocessing complexity of QST-CP. Here, n denotes the qubit count, m the truncated polynomial degree, d the number of variables, and ε the measurement error tolerance.

	Circuit depth	Repetition count	Postprocessing
Single variable	$O(n)$	$O[4m/(3\varepsilon)]$	$O(1)$
Multi variable	$O(n)$	$O[(4m/3)^d/(\varepsilon d!)]$	$O(m^d/d!)$

the complexity $O(m^d/d!)$ for evaluating the magnitude of a single quantum state.

We summarize the complexities for both single- and multivariable cases in Table I. The measurement repetition count and postprocessing complexity are independent of qubit count n. Meanwhile, the circuit depth is linear in n if the state can be prepared by a shallow circuit. This is a significant improvement over classical tomography methods requiring exponential costs. However, the complexity of QST-CP is highly dependent on the polynomial degree m. By controlling m, we can keep the overall expense manageable.

Note that various quantum errors, such as the quantum noise, quantum gate error, and finite decoherence time, can cause deviations in the measurement of expansion coefficients, which affects the reconstruction of the target function. This problem can be mitigated by advancements in quantum hardware, such as stronger noise resilience or higher quantum gate fidelities, or through algorithms such as quantum error correction codes.

IV. RESULTS

A. QST-CP of analytic functions

We evaluate QST-CP by applying it to various functions encoded in quantum states. QISKIT [52] is used to simulate the entire workflow including circuit execution and measurement on a classical computer, where the preparation circuits were

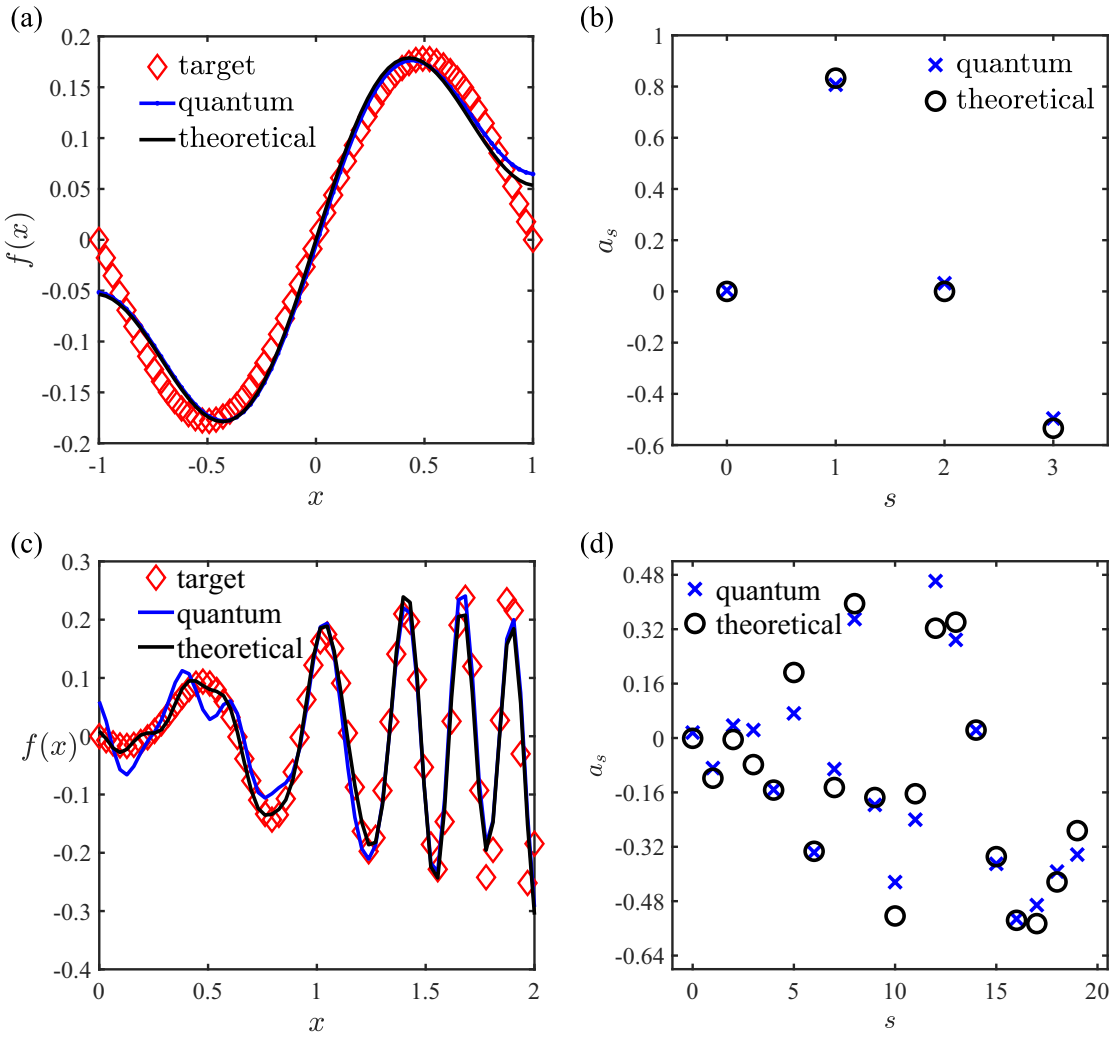

FIG. 6. Simulation results of the QST-CP method for measuring one-dimensional functions encoded with six qubits. Panels (a) and (b) show the single-mode function $f(x) = \sin(\pi x)$, while (c) and (d) show multimode function $f(x) = \log(x+1)\sin(5e^x)$. Panels (a) and (c) present the comparison among the target function, the quantum result, and the theoretical result of the expansion with the same degree of polynomials, with quantum fidelity 97.74% and 90.11% for the single- and multimode cases, respectively. Panels (b) and (d) present comparison between the expansion coefficients a_s acquired by the quantum method and theoretical calculation.

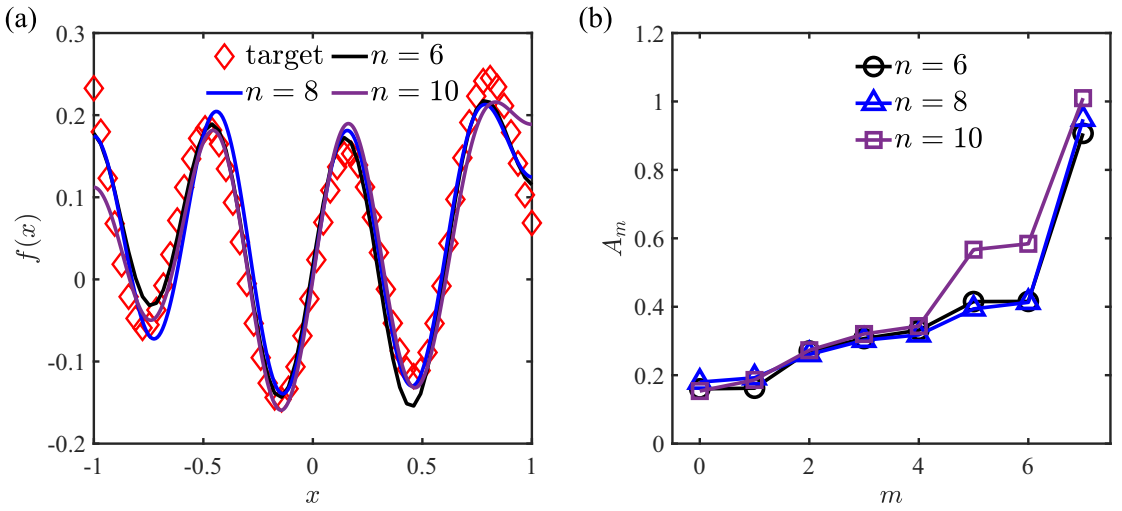

FIG. 7. Approximate tomography result of function $f(x) = x^2 + \sin(10x)$ on $[-1, 1]$ encoded with $n = 6, 8$, and 10 qubits. (a) Comparison between target function and results with different n. For clear demonstration, the function values for $n = 6$ and 8 are normalized to collapse with $n = 10$ curve. The quantum fidelities are 95.56%, 94.01%, and 93.99% for these three cases. (b) The trend of A_m for different n. The measurement ends at $m = 7$ for all three cases.

implemented using its `StatePreparation` function. In all reported results, we performed 500 measurement repetitions for each expansion coefficients.

Results for measuring a single-mode function $f(x) = \sin \pi x$ and a multimode function $f(x) = \log(x + 1)\sin(5e^x)$ with varying amplitudes, encoded using six qubits, are presented in Fig. 6. Note that all function values are normalized in the implementation to satisfy the normalization condition of a quantum state. The measurement accuracy is quantified by the quantum fidelity $|\langle f_t|f_m\rangle|^2$ between the target function state $|f_t\rangle$ and the measurement result state $|f_m\rangle$, which is defined discretely. The single- and multimode cases in Figs. 6(a) and 6(c), with manageable expansion orders $m = 3$ and $m = 19$, yield quantum fidelities of 97.74% and 90.11%, respectively, demonstrating that the method captures key features of analytic functions.

Figures 6(b) and 6(d) provide a more detailed comparison for each expansion coefficients. Most measured coefficients are close to their theoretical values calculated from Eq. (6), while some exhibit noticeable deviations, likely due to the limited 500 shots used for each coefficient. Nevertheless, the summed results still remain in good agreement with the theoretical expansion, demonstrating that QST-CP is reasonably robust against measurement-induced sampling errors, a desirable property for practical implementations on quantum hardware.

We further examine the dependence of QST-CP on the number of qubits by considering three quantum states with $n = 6$, 8, and 10, all encoding the same function $f(x) = x^2 + \sin(10x)$. Applying QST-CP with $A_c = 0.85$, the measurement results in Fig. 7 show good agreement with the target function, with quantum fidelity 95.56%, 94.01%, and 93.99%, respectively. Furthermore, the growth trends of the partial sum A_m in Fig. 7(b) show that approximations with different n all reach the threshold $A_c = 0.85$ at the same polynomial degree $m = 7$. Together with the observation in Table I that the number of measurement repetitions is independent of n, our approach avoids the classical exponential cost of QST for quantum states encoding simple functions.

Note that the partial sum A_m is calculated from measurement results, where errors are inevitable, and its value serves only as an estimation for the information fraction in the Chebyshev expansion. Furthermore, A_m provides a good enough approximation for inner product $\langle f_t|f_m\rangle$, which allows us to monitor the reconstructed function and avoid unnecessary measurement with threshold value A_c.

The relation between A_m and the inner product can be established mathematically. For clarification, here we use $\mathcal{A}_s$ to denote the theoretical expansion coefficients as in Eq. (6), and a_s to denote the measurement results of corresponding coefficients. These coefficients satisfy $|a_s - \mathcal{A}_s| \leqslant \varepsilon$, where ε is the error tolerance of quantum measurement. From the orthogonality of Chebyshev polynomials, the inner product between the target and reconstructed functions can be expressed as

$$\langle f_t|f_m\rangle = \sum_{s=0}^{m} \mathcal{A}_s^* a_s. \tag{15}$$

We can then further derive the inequality

$$\begin{aligned} |A_m - \langle f_t|f_m\rangle| &= \left|\sum_{s=0}^{m}(|a_s|^2 - \mathcal{A}^* a_s)\right| = \sum_{s=0}^{m}|a_s||a_s^* - \mathcal{A}_s^*| \\ &= \sum_{s=0}^{m}|a_s||a_s - \mathcal{A}| \leqslant \sum_{s=0}^{m}\varepsilon|a_s| \\ &\leqslant (m+1)\varepsilon \max_{s\leqslant m}|a_s|. \end{aligned} \tag{16}$$

This implies that A_m provides an approximation for inner product $\langle f_t|f_m\rangle$ whose actual value can fluctuate due to measurement deviations. The partial sum is then used to monitor the measurement progress and determine the stopping point.

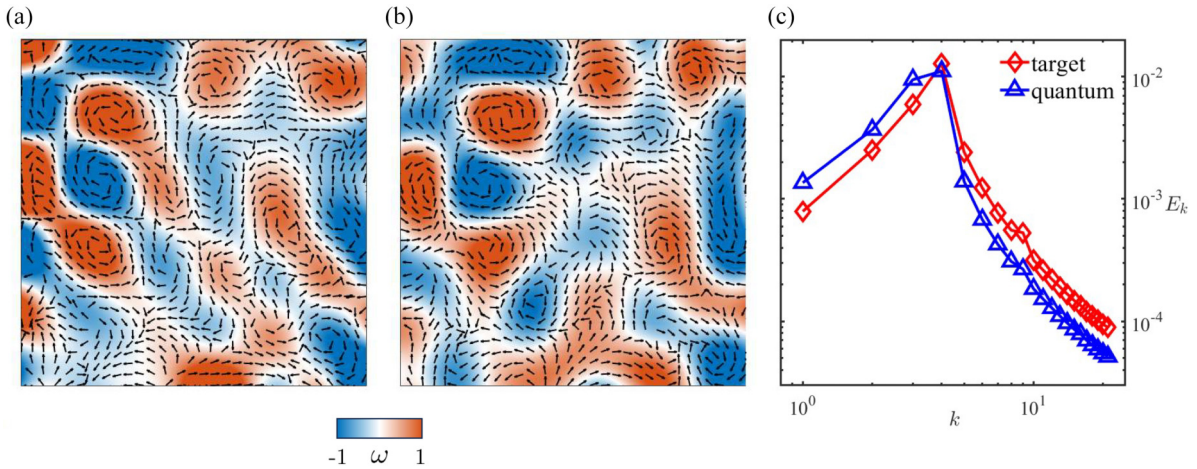

FIG. 8. Comparison between (a) a snapshot of the 2D DNS velocity field (arrows) and vorticity contour and (b) the corresponding quantum measuring results on a 64×64 grid (corresponding to 12 qubits) with threshold $A_c = 0.5$ and polynomial order $m = 11$. The quantum fidelity is 78.42%. (c) Comparison of the energy spectra for the two velocity fields.

B. QST-CP of numerically simulated flow fields

We evaluate QST-CP on two-dimensional (2D) vortical flows from numerical simulations, expressed as $f(x, y) = u_x(x, y) + iu_y(x, y)$ with velocity components u_x and u_y. The flow field is generated by solving the 2D Navier-Stokes (NS) equations for homogeneous isotropic turbulence using a standard pseudo-spectral method, and the resulting data are encoded into quantum states. As a representative case, we analyze a 2D velocity field from direct numerical simulation (DNS). The simulation is calculated by pseudospectral method [53] on a $[0, 2\pi]^2$ domain discretized with 1024^2 grid points under periodic boundary conditions. The velocity field exhibits a Taylor Reynolds number of $\mathrm{Re}_\lambda = 122.9$. The field is downsampled from 1024^2 to 64^2 uniform grid points, corresponding to 12 qubits. Figures 8(a) and 8(b) compare the DNS reference field with the quantum reconstruction, where the vorticity magnitude is defined by $\omega = \partial u_y/\partial x - \partial u_x/\partial y$. With the threshold parameter set to $A_c = 0.5$, the measurement

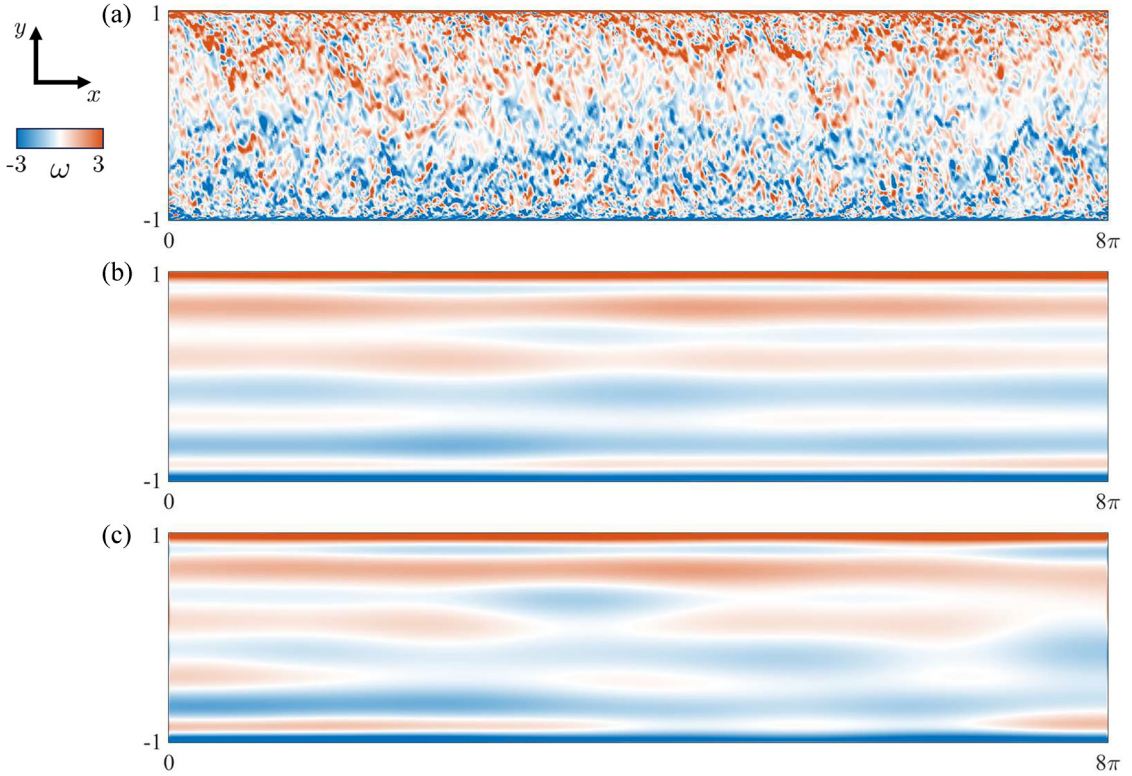

FIG. 9. Result of quantum measuring an x-y section of turbulent channel flow with 512×128 uniform grid points (corresponding to 16 qubits). (a) Target flow field from DNS data. (b) Quantum measuring result with $A_c = 0.9$, leading to $m = 11$. (c) Theoretical expansion result at the same polynomial order. The quantum fidelity between quantum and theoretical results is 84.33%.

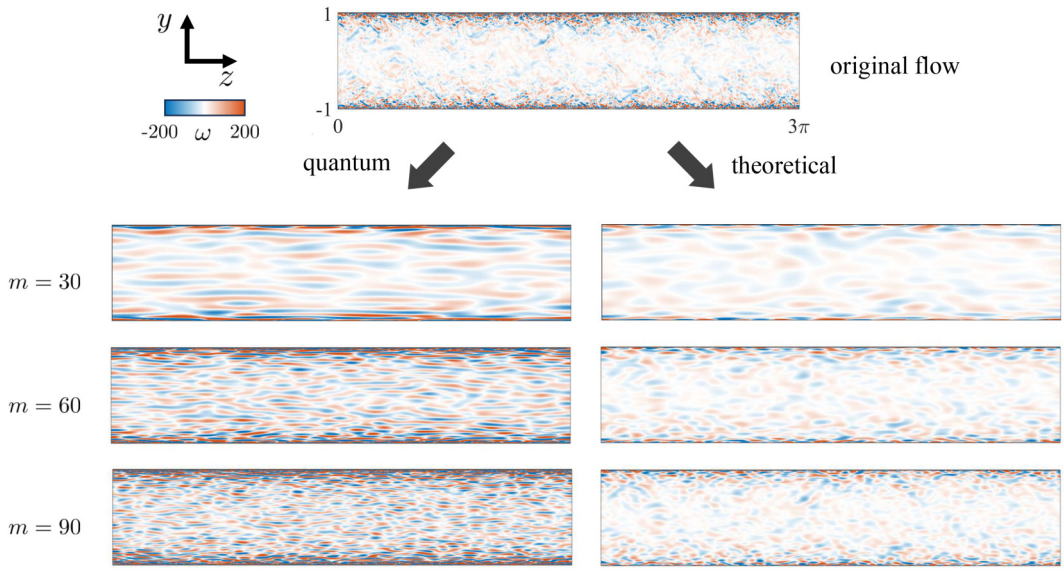

FIG. 10. Result of quantum measuring a z-y section of turbulent channel flow with 512×128 uniform grid points (corresponding to 16 qubits). Quantum results of three polynomial degrees $m = 30$, 60, and 90 are provided on the left column, with theoretical results on the right column.

terminates at polynomial order $m = 11$. The reconstruction reproduces the dominant large-scale vortex structures, which is further supported by the agreement of the energy spectra shown in Fig. 8(c), demonstrating the capability of the method to recover the major features of complex flow fields.

To further assess the method, we consider a turbulent channel flow field from the Johns Hopkins Turbulence Database [54], simulated in a domain of $8\pi \times 2 \times 3\pi$ at a friction Reynolds number of 1000. We extract x-y and z-y sections and resample them onto 512×128 grid points, corresponding to 16 qubits, where x, y, and z denote the streamwise, wall-normal, and spanwise directions, respectively. Figure 9(a) shows the target x-y section at $z = 1.5\pi$, while Figs. 9(b) and 9(c) present the reconstructions, with Fig. 9(b) obtained from the QST-CP procedure using a threshold of $A_c = 0.9$ and polynomial order $m = 11$, and Fig. 9(c) from the theoretical expansion at the same order, highlighting the large-scale mode of the target flow field. The quantum reconstruction with a low polynomial degree attains a fidelity of 84.33% relative to the theoretical result, effectively reproducing the dominant streamwise flow and the strong boundary vortex sheet that characterize the channel flow.

This property is further elaborated on in the case of z-y section, where $x = 4\pi$ and the target function is expressed as $f(y, z) = u_z(y, z) + iu_y(y, z)$, as demonstrated in Fig. 10. In the absence of the primary flow in the x direction, the finer structures emerge as the dominant flow features. We provide reconstruction results for different polynomial degrees $m = 30$, 60, and 90, with quantum results on the left column and theoretical results on the right. Increasing the polynomial degree progressively resolves smaller-scale features and captures richer spectral content, indicating that, by tuning the threshold value, QST-CP offers flexible control over spatial resolution to accommodate different application requirements. Lower A_c values yield efficient approximate representations, whereas higher A_c values enable high-resolution reconstructions that capture detailed flow characteristics.

V. CONCLUSION

We propose QST-CP, a spectral method for an approximate tomography of pure quantum states encoding continuous functions, formulated in Eqs. (6) and (7). The advantage lies in its scale-sensitive truncation, as Chebyshev modes provide a scale interpretation and low-order terms capture large-scale structures, allowing proper stopping that preserves dominant features while reducing measurement overhead. By reformulating tomography as an estimation of a set of expansion coefficients via inner product between the target quantum state and the Chebyshev bases, implemented using the circuits in Figs. 2 and 3, and reconstructing a truncated series, the QST-CP method achieves polynomial scaling in circuit depth, with measurement repetitions and postprocessing independent of qubit count. Furthermore, a stopping criterion based on the cumulative coefficient energy in Eq. (11) establishes the accuracy-efficiency trade-off and specifies a termination rule.

We evaluate QST-CP from analytic functions to complex flow fields. For analytic functions, the method yields accurate reconstructions with modest expansion orders, regardless of the numbers of qubits used in quantum state preparation. This confirms that the quality of reconstruction remains stable as the qubit count increases, highlighting the method's scalability in addressing more complex systems. The complexity analysis in Table I further reveals that the number of measurement repetitions and complexity of post-processing is independent of the qubit count, outperforming the exponential scaling typical of classical QST. For more complicated velocity fields, the method efficiently captures dominant flow structures in both isotropic turbulence and channel-flow sections with controlled expansion orders. Increasing the

expansion order reveals finer-scale details, illustrating a balance between efficiency and accuracy for QST by adjusting the truncation length of the polynomial series.

The QST-CP is tailored for extracting large-scale modes from quantum states and partly addresses the output problem by enabling rapid data readout for many quantum computing applications. Though various measurement errors such as quantum noise, quantum gate errors, and finite decoherence time can affect the accuracy of function reconstruction, the algorithm can be applied without theoretical restrictions by incorporating a control qubit and the appending polynomial preparation circuit, where a shallow circuit depth ensures high efficiency.

In future work, the development of more efficient circuits for inner product measurement could reduce the reliance of overall depth and control overhead on preparation of both the target state and the polynomial basis, thereby facilitating practical deployment on quantum hardware. Integration with quantum partial differential equation solvers, where the spectral QST module is treated as a readout head for variational or block encoding solvers, could enable direct recovery of coarse solutions in quantum computations. Moreover, advances in quantum hardware, such as higher gate fidelities or better noise resilience, as well as quantum error correction algorithms could improve the accuracy and stability of our method.

ACKNOWLEDGMENTS

This work wassupported, in part, by the National Natural Science Foundation of China (Grants No. 12432010, No. 12525201, No. 12302294, and No. 12588201), the National Key R&D Program of China (Grant No. 2023YFB4502600), and the New Cornerstone Science Foundation through the XPLORER Prize.

DATA AVAILABILITY

The data that support the findings of this article are openly available [48].

APPENDIX: GENERALIZATION OF QST-CP TO DENSITY MATRIX

We discuss the theoretical possibility of generalizing our QST-CP framework to density matrix. We recall that quantum states $\{|T_{s,n}\rangle|0 \leqslant s \leqslant 2^n - 1\}$ form an orthonormal Chebyshev basis of n-qubit quantum state. Any density matrix ρ can be expressed under both the computational basis and the Chebyshev basis as

$$\rho = \sum_{p=0}^{2^n-1}\sum_{q=0}^{2^n-1} \rho_{pq}|p\rangle\langle q| = \sum_{s=0}^{2^n-1}\sum_{t=0}^{2^n-1} \tilde{\rho}_{st}|T_{s,n}\rangle\langle T_{t,n}|, \tag{A1}$$

where ρ_{pq} and $\tilde{\rho}_{st}$ are the corresponding matrix elements.

Equation (A1) is closely related to our QST-CP method for functions of two variables. We consider the density matrix elements in the computational basis as the function values at discrete grid points. Accordingly, we define a target function $f(x_1, x_2)$ as in Eq. (1), which satisfies $f(X_{2^n,p}, X_{2^n,q}) = \rho_{pq}$. Application of the Chebyshev expansion as in Eq. (7) to $f(x_1, x_2)$ yields

$$f(x_1, x_2) = \sum_{s=0}^{2^n-1}\sum_{t=0}^{2^n-1} \tilde{\rho}_{st}\tilde{T}_{s,2^n}(x_1)\tilde{T}_{t,2^n}(x_2), \tag{A2}$$

suggesting that it is feasible to approximately reconstruct the full density matrix with less complexity by measurement of low-order terms of $\tilde{\rho}_{st}$, which can be achieved by recently developed techniques such as direct weak tomography and direct strong tomography [55–57]. These results imply the possibility of applying QST-CP framework to density matrices.

However, it is still worth exploring whether this generalization to density matrices can be utilized in practical problems, as density matrices should follow hermitianity or positive semi-definitiveness. Possible applications include quantum state produced from preparation circuit with decoherent noise, where it turns into a mixed state close to the original pure state. If the effect of decoherence can be bounded mathematically, then it might be possible to extract original function information from density matrices. Another application can be established with a linear combination of unitaries, where a mixed state with the form of $\rho = \sum_i |f_i\rangle\langle f_i|$ is applied to avoid the complexity of controlled rotation gates. In these scenarios, the mathematical constraints on the density matrices are naturally satisfied.

[1] M. A. Nielsen, I. L. Chuang, *Quantum Computation and Quantum Information* (Cambridge University Press, Cambridge, England, 2010).

[2] P. Wittek, *Quantum Machine Learning: What Quantum Computing Means to Data Mining* (Academic Press, New York, 2014).

[3] Y. Cao, J. Romero, J. P. Olson, M. Degroote, P. D. Johnson, M. Kieferová, I. D. Kivlichan, T. Menke, B. Peropadre, N. P. D. Sawaya, *et al.*, Quantum chemistry in the age of quantum computing, Chem. Rev. **119**, 10856 (2019).

[4] S. Jin, N. Liu, and Y. Yu, Quantum simulation of partial differential equations: Applications and detailed analysis, Phys. Rev. A **108**, 032603 (2023).

[5] Z. Meng, J. Zhong, S. Xu, K. Wang, J. Chen, F. Jin, X. Zhu, Y. Gao, Y. Wu, C. Zhang, N. Wang, Y. Zou, A. Zhang, Z. Cui, F. Shen, Z. Bao, Z. Zhu, Z. Tan, T. Li, P. Zhang, *et al.*, Simulating unsteady fluid flows on a superconducting quantum processor, Commun. Phys. **7**, 349 (2024).

[6] Y. Xiao, L. M. Yang, C. Shu, S. C. Chew, B. C. Khoo, Y. D. Cui, and Y. Y. Liu, Physics-informed quantum neural network for solving forward and inverse problems of partial differential equations, Phys. Fluids **36**, 097145 (2024).

[7] S. Succi, W. Itani, K. Sreenivasan, and R. Steijl, Quantum computing for fluids: Where do we stand? Europhys. Lett. **144**, 10001 (2023).

[8] S. S. Bharadwaj and K. R. Sreenivasan, Towards simulating fluid flows with quantum computing, Sādhanā **50**, 57 (2025).

[9] F. Tennie, S. Laizet, S. Lloyd, and L. Magri, Quantum computing for nonlinear differential equations and turbulence, Nat. Rev. Phys. **7**, 220 (2025).

[10] Z. Y. Meng, C. Song, and Y. Yang, Challenges of simulating fluid flows on near-term quantum computer, Sci. China Phys. Mech. Astron. **68**, 104705 (2025).

[11] R. Steijl and G. N. Barakos, Parallel evaluation of quantum algorithms for computational fluid dynamics, Comput. Fluids **173**, 22 (2018).

[12] F. Gaitan, Finding flows of a Navier-Stokes fluid through quantum computing, npj Quantum Inf. **6**, 61 (2020).

[13] M. Lubasch, J. Joo, P. Moinier, M. Kiffner, and D. Jaksch, Variational quantum algorithms for nonlinear problems, Phys. Rev. A **101**, 010301(R) (2020).

[14] N. Gourianov, M. Lubasch, S. Dolgov, Q. Y. van den Berg, H. Babaee, P. Givi, M. Kiffner, and D. Jaksch, A quantum-inspired approach to exploit turbulence structures, Nat. Comput. Sci. **2**, 30 (2022).

[15] P. Pfeffer, F. Heyder, and J. Schumacher, Hybrid quantum-classical reservoir computing of thermal convection flow, Phys. Rev. Res. **4**, 033176 (2022).

[16] J. Zylberman, G. D. Molfetta, M. Brachet, N. F. Loureiro, and F. Debbasch, Quantum simulations of hydrodynamics via the Madelung transformation, Phys. Rev. A **106**, 032408 (2022).

[17] K. Fukagata, Towards quantum computing of turbulence, Nat. Comput. Sci. **2**, 68 (2022).

[18] Z. Y. Meng and Y. Yang, Quantum computing of fluid dynamics using the hydrodynamic Schrödinger equation, Phys. Rev. Res. **5**, 033182 (2023).

[19] Z. Y. Meng and Y. Yang, Quantum spin representation for the Navier-Stokes equation, Phys. Rev. Res. **6**, 043130 (2024).

[20] D. Jaksch, P. Givi, A. J. Daley, and T. Rung, Variational quantum algorithms for computational fluid dynamics, AIAA J. **61**, 1885 (2023).

[21] Y. Liu, Z. Chen, C. Shu, P. Rebentrost, Y. Liu, S. Chew, B. Khoo, and Y. Cui, A variational quantum algorithm-based numerical method for solving potential and Stokes flows, Ocean Eng. **292**, 116494 (2024).

[22] Z. Y. Chen, T. Y. Ma, C. C. Ye, L. Xu, W. Bai, L. Zhou, M. Y. Tan, X. N. Zhuang, X. F. Xu, and Y. J. Wang, Enabling large-scale and high-precision fluid simulations on near-term quantum computers, Comput. Methods Appl. Mech. Eng. **432**, 117428 (2024).

[23] S. S. Bharadwaj and K. R. Sreenivasan, Hybrid quantum algorithms for flow problems, Proc. Natl. Acad. Sci. USA **120**, e2311014120 (2023).

[24] W. Itani, K. R. Sreenivasan, and S. Succi, Quantum algorithm for lattice Boltzmann (QALB) simulation of incompressible fluids with a nonlinear collision term, Phys. Fluids **36**, 017112 (2024).

[25] B. Y. Wang, Z. Y. Meng, Y. M. Zhao, and Y. Yang, Quantum lattice Boltzmann method for simulating nonlinear fluid dynamics, arXiv:2502.16568.

[26] D. Gross, Y. K. Liu, S. T. Flammia, S. Becker, and J. Eisert, Quantum state tomography via compressed sensing, Phys. Rev. Lett. **105**, 150401 (2010).

[27] C. A. Riofrio, D. Gross, S. T. Flammia, T. Monz, D. Nigg, R. Blatt, and J. Eisert, Experimental quantum compressed sensing for a seven-qubit system, Nat. Commun. **8**, 15305 (2017).

[28] K. Banaszek, G. M. D'ariano, M. G. A. Paris, and M. F. Sacchi, Maximum-likelihood estimation of the density matrix, Phys. Rev. A **61**, 010304(R) (1999).

[29] J. W. Shang, Z. Y. Zhang, and H. K. Ng, Superfast maximum-likelihood reconstruction for quantum tomography, Phys. Rev. A **95**, 062336 (2017).

[30] C. Ferrie, Self-guided quantum tomography, Phys. Rev. Lett. **113**, 190404 (2014).

[31] E. Bolduc, G. C. Knee, E. M. Gauger, and J. Leach, Projected gradient descent algorithms for quantum state tomography, npj Quantum Inf. **3**, 44 (2017).

[32] G. Torlai and R. G. Melko, Machine-learning quantum states in the NISQ era, Annu. Rev. Condens. Matter Phys. **11**, 325 (2020).

[33] S. Ahmed, M. C. Sanchez, F. Nori, and A. F. Kockum, Quantum state tomography with conditional generative adversarial networks, Phys. Rev. Lett. **127**, 140502 (2021).

[34] D. Koutný, L. Motka, Z. Hradil, J. Řeháček, and L. L. Sanchez Soto, Neural-network quantum state tomography, Phys. Rev. A **106**, 012409 (2022).

[35] B. Qi, Z. B. Hou, L. Li, D. Y. Dong, G. Y. Xiang, and G. C. Guo, Quantum state tomography via linear regression estimation, Sci. Rep. **3**, 3496 (2013).

[36] Z. B. Hou, H. S. Zhong, Y. Tian, D. Y. Dong, B. Qi, L. Li, Y. L. Wang, F. Nori, G. Y. Xiang, C. F. Li, *et al.*, Full reconstruction of a 14-qubit state within four hours, New J. Phys. **18**, 083036 (2016).

[37] B. Qi, Z. B. Hou, Y. L. Wang, D. Y. Dong, H. S. Zhong, L. Li, G. Y. Xiang, H. M. Wiseman, C. F. Li, and G. C. Guo, Adaptive quantum state tomography via linear regression estimation: Theory and two-qubit experiment, npj Quantum Inf. **3**, 19 (2017).

[38] H. Y. Huang, R. Kueng, and J. Preskill, Predicting many properties of a quantum system from very few measurements, Nat. Phys. **16**, 1050 (2020).

[39] J. Cotler and F. Wilczek, Quantum overlapping tomography, Phys. Rev. Lett. **124**, 100401 (2020).

[40] Y. Liu, D. Y. Wang, S. C. Xue, A. Q. Huang, X. Fu, X. G. Qiang, P. Xu, H. L. Huang, M. T. Deng, C. Guo, X. Yang and J. Wu, Variational quantum circuits for quantum state tomography, Phys. Rev. A **101**, 052316 (2020).

[41] A. Steffens, C. A. Riofrío, W. McCutcheon, I. Roth, B. A. Bell, A. McMillan, M. S. Tame, J. G. Rarity, and J. Eisert, Experimentally exploring compressed sensing quantum tomography, Quantum Sci. Technol. **2**, 025005 (2017).

[42] M. Cramer, M. B. Plenio, S. T. Flammia, R. Somma, D. Gross, S. D. Bartlett, O. L. Cardinal, D. Poulin, and Y. K. Liu, Efficient quantum state tomography, Nat. Commun. **1**, 149 (2010).

[43] B. P. Lanyon, C. Maier, M. Holzäpfel, T. Baumgratz, C. Hempel, P. Jurcevic, I. Dhand, A. S. Buyskikh, A. J. Daley, M. Cramer, *et al.*, Efficient tomography of a quantum many-body system, Nat. Phys. **13**, 1158 (2017).

[44] T. Kosugi, S. Daimon, H. Nishi, S. Tsuneyuki, and Y. I. Matsushita, Qubit encoding for a mixture of localized functions, Phys. Rev. A **110**, 062407 (2024).

[45] T. Kosugi, X. Huang, H. Nishi, and Y. I. Matsushita, Tensor-decomposition technique for qubit encoding of

maximal-fidelity Lorentzian orbitals in real-space quantum chemistry, Phys. Rev. A **111**, 052615 (2025).

[46] O. Kyriienko, A. E. Paine, and V. E. Elfving, Solving nonlinear differential equations with differentiable quantum circuits, Phys. Rev. A **103**, 052416 (2021).

[47] A. Sarma, T. W. Watts, M. Moosa, Y. Liu, and P. L. McMahon, Quantum variational solving of nonlinear and multidimensional partial differential equations, Phys. Rev. A **109**, 062616 (2024).

[48] Codes available at https://github.com/YYgroup/ChebyMeasure, 2025.

[49] A. N. Kolmogorov, The local structure of turbulence in incompressible viscous fluid for very large Reynolds numbers, Proc. A **434**, 9 (1991).

[50] T. J. Rivlin, *Chebyshev Polynomials* (Courier Dover, New York, 2020).

[51] L. N. Trefethen, *Approximation Theory and Approximation Practice, Extended Edition* (SIAM, Philadelphia, PA, 2019).

[52] A. J. Abhari, M. Treinish, K. Krsulich, C. J. Wood, J. Lishman, J. Gacon, S. Martiel, P. D. Nation, L. S. Bishop, A. W. Cross, B. R. Johnson, and J. M. Gambetta, Quantum computing with Qiskit, arXiv:2405.08810.

[53] S. A. Orszag, Numerical methods for the simulation of turbulence, Phys. Fluids **12**, II-250 (1969).

[54] J. Graham, K. Kanov, X. I. A. Yang, M. K. Lee, N. Malaya, C. C. Lalescu, R. Burns, G. Eyink, A. Szalay, R. D. Moser, and C. Meneveau, A web services accessible database of turbulent channel flow and its use for testing a new integral wall model for LES, J. Turbul. **17**, 181 (2016).

[55] J. S. Lundeen, B. Sutherland, A. Patel, C. Stewart, and C. Bamber, Direct measurement of the quantum wavefunction, Nature (London) **474**, 188 (2011).

[56] C. R. Zhang, M. J. Hu, Z. B. Hou, J. F. Tang, J. Zhu, G. Y. Xiang, C. F. Li, G. C. Guo, and Y. S. Zhang, Direct measurement of the two-dimensional spatial quantum wave function via strong measurements, Phys. Rev. A **101**, 012119 (2020).

[57] L. Xu, M. T. Zhou, R. Tao, Z. Zhong, B. Wang, Z. Y. Cao, H. Xia, Q. Wang, H. Zhan, A. Zhang, S. Yu, N. Xu, Y. Dong, C. Ren, and L. Zhang, Resource-efficient direct characterization of general density matrix, Phys. Rev. Lett. **132**, 030201 (2024).